ADVANCED FUNCTIONAL MATERIALS
www.afm-journal.de

Materials Views
www.MaterialsViews.com

New Ternary Europium Aluminate Luminescent Nanoribbons for Advanced Photonics

*Feng Liu, John D. Budai, Xufan Li, Jonathan Z. Tischler, Jane Y. Howe, Chengjun Sun, Richard S. Meltzer, and Zhengwei Pan**

Developing novel one-dimensional (1D) luminescent nanostructures (e.g., nanowires and nanoribbons) is highly desired for enabling progress in nanophotonics and other emerging optical technologies. Previous studies on 1D luminescent nanostructures were mostly focused on elemental and binary semiconductor materials, the light emission of which originates from the radiative recombination of electrons and holes via either intrinsic states or extrinsic defect states. Herein, three kinds of ternary europium aluminate nanoribbons are reported that have localized Eu^{2+} luminescent centers and exhibit new compositions, new crystal lattice structures, and new luminescence properties and mechanisms. These three europium aluminate nanoribbons are: blue luminescent $EuAl_6O_{10}$ with a new composition and a new tetragonal lattice structure, green luminescent $EuAl_2O_4$ with a monoclinic lattice structure, and orange luminescent $EuAl_2O_4$ with a new hexagonal lattice structure and extremely large band width and Stokes shift of emission. These materials have promising applications as nanometer-scale light generators and waveguides in nanophotonics and as light converting phosphors in warm white light-emitting diodes.

1. Introduction

One-dimensional (1D) luminescent nanomaterials, such as semiconductor nanowires and semiconducting oxide nanoribbons, have been proven to be attractive, versatile and powerful building blocks for the bottom-up assembly of a variety of nanoscale photonic systems, including light-emitting diodes (LED),[1,2] lasers,[3,4] sensors,[5,6] and photonic circuitry.[7,8] Among these nanowire-based systems, photonic circuitry constructed from nanowires (e.g., ZnO) and nanoribbons (e.g., SnO_2) is receiving considerable attention because it offers numerous opportunities for the development of next-generation optical information processors.[8] The work of assembling nanowire/nanoribbon building blocks with different functions, such as light creation, routing, and detection, marks the first step toward achieving photonic circuits that can manipulate light pulses within submicrometer dimensions. If these waveguide components can be integrated into a fully functional photonic circuit, highly integrated light-based devices, such as photonic computers, can be realized. Limited by the optical performance of the building blocks, however, further development of the nanostructured circuitry may be constrained. For example, the visible emissions from ZnO (green light at ≈530 nm) and SnO_2 (green light at ≈500 nm and orange light at ≈590 nm) originate directly from defect state energy levels,[8] resulting in inconsistent optical performance for nanoribbons/nanowires synthesized in different batches. To overcome such material-related constraints, new types of luminescent nanostructures that can emit light from diverse localized luminescent centers in materials are highly desired. In this regard, rare earth-activated luminescent materials, whose luminescence is usually determined by the nature of rare earth luminescent centers,[9] apparently meet this material demand.

Rare earth ion-activated phosphors are one of the most important families of luminescent materials, and are being widely used in many important fields involving lighting, display, optical communication, laser, and biological imaging.[9–12] Among the rare earth ions, divalent europium ions, Eu^{2+}, are receiving increasing attention for their remarkable optical performance in solids.[13–18] For example, the typical broadband emissions from Eu^{2+} ions (generally attributed to inter-configurational $4f^65d \rightarrow 4f^7$ transitions) in different hosts can be tuned from near-ultraviolet (UV) to red, while the excitation can be extended from blue light to the X-ray region.[13] Eu^{2+}-activated phosphors associated with different luminescence colors have contributed to many practical applications including solid-state

Dr. F. Liu, X. F. Li, Prof. Z. W. Pan
College of Engineering
University of Georgia
Athens, GA 30602, USA
E-mail: panz@uga.edu
Dr. F. Liu, Prof. R. S. Meltzer, Prof. Z. W. Pan
Department of Physics and Astronomy
University of Georgia
Athens, GA 30602, USA
Dr. J. D. Budai, Dr. J. Z. Tischler, Dr. J. Y. Howe
Materials Science and Technology Division
Oak Ridge National Laboratory
Oak Ridge, TN 37831, USA
Dr. C. J. Sun
X-ray Science Division
Argonne National Laboratory
Argonne, IL 60439, USA

DOI: 10.1002/adfm.201202539

lighting and display backlights.[14,15] Furthermore, photoionization and electron transfer phenomena followed by Eu^{2+} $4f^65d \rightarrow 4f^7$ emission in some Eu^{2+}-activated phosphors have led to such important applications as X-ray storage phosphors,[16] long-persistent luminescence,[17] and radiation detection.[18] These diverse optical properties suggest that if the Eu^{2+}-activated luminescent materials can be integrated into nanowires or nanoribbons, it will provide a broad range of luminescent nanostructured building blocks for fabricating photonic circuits with enhanced functionalities. This capability could significantly advance the emerging field of nanophotonics. However, no Eu^{2+}-activated luminescent nanowires or nanoribbons are currently available for nanophotonics.

Here we report three kinds of Eu^{2+}-activated ternary europium aluminate nanoribbons that exhibit new compositions, new crystal lattice structures, and new luminescence properties and mechanisms.[19] These three europium aluminate nanoribbons are: blue luminescent $EuAl_6O_{10}$ with a new composition and a new tetragonal lattice structure, green luminescent $EuAl_2O_4$ with a monoclinic lattice structure, and orange luminescent $EuAl_2O_4$ with a new hexagonal lattice structure and extremely large band width and Stokes shift of emission. These materials have very promising applications as nanoscale light generators and waveguides in photonic circuitry and as light converting phosphors in white light-emitting diodes (LEDs).

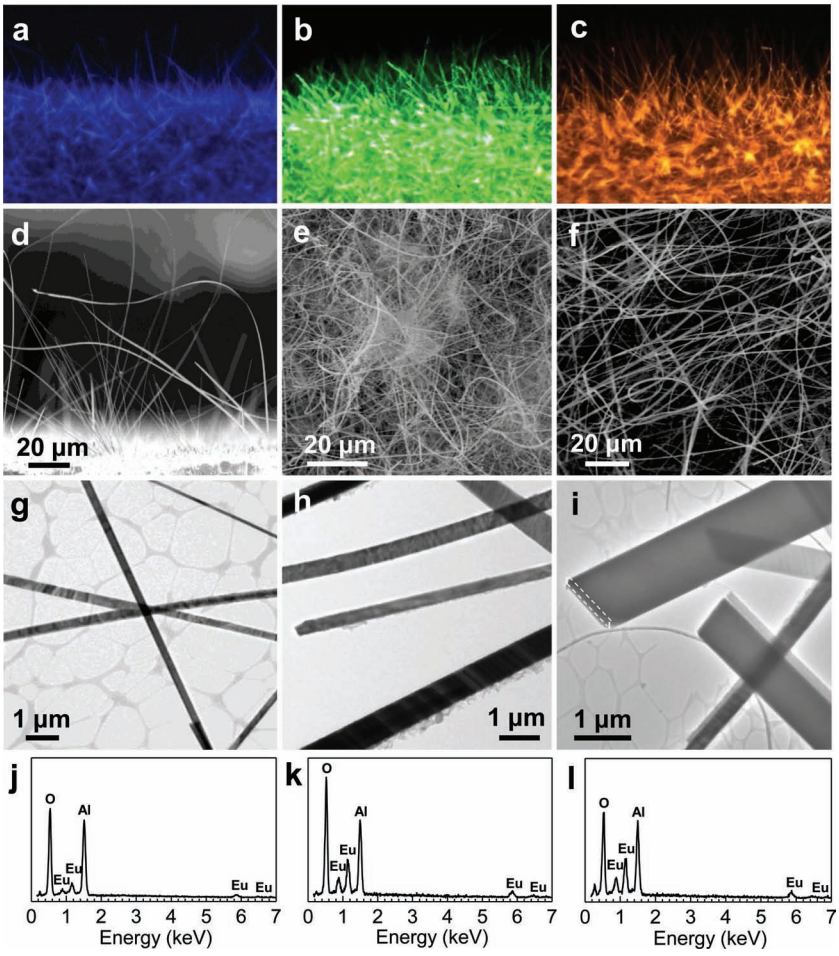

Figure 1. Morphologies and compositions of EAO nanoribbons. a–c) Optical images of blue, green, and orange luminescent EAO nanoribbons taken under a digital optical microscope with a 365 nm UV lamp excitation. d–f) SEM images of blue, green, and orange luminescent EAO nanoribbons. g–i) TEM images of blue, green, and orange luminescent EAO nanoribbons. The white dashed rectangle in i) indicates the rectangular cross section of the end of a ribbon. j–l) EDS spectra of blue, green, and orange luminescent EAO nanoribbons.

2. Results and Discussion

2.1. Controlled Synthesis of Blue, Green, and Orange Luminescent Nanoribbons

The synthesis was carried out in a well-controlled tube furnace system (Figure S1a, Supporting Information) by carbothermal reaction and evaporation of a mixture of Eu_2O_3, Al_2O_3 and graphite powders (see the Experimental Section). In order to obtain the Eu^{2+}-activated europium aluminate nanoribbons, the synthesis conditions need to be strictly controlled and three prerequisites must be met: first, the base vacuum of the entire system must reach 2×10^{-3} Torr or better (to eliminate oxygen); second, graphite powder must be added for carbothermal reduction of the source oxide powders (to efficiently provide Eu^{2+}- and Al^{3+}-containing species); and third, the environment inside the reaction chamber must be weakly reducing (to create Eu ions in a divalent state). Otherwise, no luminescent nanoribbons will be grown. In a typical run, source powders with Eu_2O_3/Al_2O_3/graphite mass ratio of ≈0.6/0.1/1 were heated at 1450 °C under a pressure of 5 Torr and an argon flow rate of 50 sccm (standard cubic centimeters per minute) for 2 h. Due to the influence of the temperature gradient at the furnace hearth region, two different luminescence-color (under UV excitation) products were obtained: orange luminescent product formed in the 1200–1400 °C region and green luminescent material grown in the 1000–1200 °C region (Figure S1b, Supporting Information). When more Al_2O_3 powder was added to the source (e.g., changing the Eu_2O_3/Al_2O_3/graphite mass ratio to ≈0.6/0.5/1) and the pressure was increased to 10–15 Torr, the growth of orange and green luminescent products was suppressed; instead, a third kind of blue luminescent product was grown in the whole growth region from 1000 to 1400 °C (Figure S1c, Supporting Information). Optical microscope observations (**Figure 1**a–c) show that all the three luminescent products are wire-like and under the illumination of a 365 nm UV lamp each individual wire emits uniform photoluminescence (PL) along its entire length.

2.2. Morphology and Compositions of EAO Nanoribbons

Figure 1d–f shows scanning electron microscope (SEM) images of the blue, green, and orange luminescent wires. The wires have typical lengths in the range of several tens to several hundreds of micrometers; some even have lengths on the order of millimeters. Transmission electron microscope (TEM) images (Figure 1g–i) reveal that the wire-like structures actually have a geometrical ribbon shape and possesses a rectangular cross section.[20] Each ribbon has a uniform width and thickness along its entire length, and the typical widths and thicknesses of the ribbons are in the range of 200–1000 nm and 50–300 nm, respectively. These size ranges are optimal for efficient steering of UV and visible light for nanophotonic applications.[8]

Composition analyses using energy-dispersive X-ray spectroscopy (EDS) in an SEM showed that all three kinds of luminescent ribbons are composed of Eu, Al and O (Figure 1j–l), and these constituent elements are uniformly distributed along each ribbon (Figure S2, Supporting Information). The Eu:Al ratio in the blue luminescent ribbon is 1:6, while the values in the green and orange luminescent ribbons are approximately the same, with a ratio of 1:2. X-ray absorption near edge structure (XANES) measurement on the Eu L_3 edge carried out at the Advanced Photon Source (APS) beamline 20-BM-B[21] revealed that the Eu ions in all three products are in the divalent states (Figure S3, Supporting Information). The XANES results are consistent with the reducing synthesis environment and the broadband PL emissions (refer to **Figure 4**; detailed spectral properties will be discussed later) that typically originate from Eu^{2+} ions.[13] We therefore infer that all three kinds of luminescent ribbons are concentrated europium aluminates with europium in the divalent state (the perturbed Eu^{2+} sites are responsible for light emission in the fully concentrated phosphors).[22] Thus, the chemical formulas of the three europium aluminates can be written as $EuAl_6O_{10}$ for the blue luminescent aluminate (called *b*-EAO hereafter), $EuAl_2O_4$ for the green luminescent aluminate (called *g*-EAO), and also $EuAl_2O_4$ for the orange luminescent aluminate (called *o*-EAO). Among these three EAOs, the blue luminescent $EuAl_6O_{10}$ is a new compound. $EuAl_2O_4$ has been previously fabricated in the form of bulk powder by a solid-state reaction of Eu_2O_3 and Al_2O_3 powders;[22] however, only green PL was reported at room temperature. In this regard, the orange luminescent $EuAl_2O_4$ is also a new compound.

2.3. Determination of Crystal Structures of EAO Nanoribbons

The crystal structures of the three EAO ribbons were initially examined by conventional X-ray powder diffraction (XRD, λ = 1.5406 Å). **Figure 2**a–c shows the XRD patterns of the three EAO ribbons. By searching the ICDD (International Centre for Diffraction Data) database, we can index *g*-EAO (Figure 2b) as monoclinic $EuAl_2O_4$ because its pattern is in good agreement with that of the isostructural monoclinic $SrAl_2O_4$ (JCPDS #34-0379). The successful indexation of *g*-EAO confirms the valence state of europium (i.e., Eu^{2+}) and thus supports the chemical formulas of the EAOs. However, no corresponding phases or isostructural phases were found for *b*-EAO (Figure 2a) and *o*-EAO (Figure 2c) in the ICDD database or other commonly available databases such as the Inorganic Crystal Structure Database. To determine the crystal structures of *b*-EAO and *o*-EAO, we then used a combination of high-resolution synchrotron X-ray powder diffraction (λ = 0.414 Å; monochromatic energy, 29.9 keV) at the APS beamline 11-BM-B[23] and polychromatic Laue microdiffraction at the APS beamline 34-ID-E.[24–26] Figure 2d,e show the synchrotron powder diffraction patterns from *b*-EAO and *o*-EAO ribbons, respectively (the related diffraction data are given, respectively, in Figure S4 and Figure S5 of the Supporting Information), which coincide, respectively, with the conventional X-ray diffraction patterns shown in Figure 2a,c very well. The phase and lattice parameters that best matched the powder measurements were identified using JADE diffraction analysis software (Materials Data, Inc.). The analyses show that the *b*-EAO ($EuAl_6O_{10}$) structure can be described as a new tetragonal phase with lattice parameters of $a = b = 7.77$ Å and $c = 17.30$ Å, while the *o*-EAO ($EuAl_2O_4$) possesses a new hexagonal structure with lattice parameters of $a = b = 6.15$ Å and $c = 10.57$ Å. (Note that these lattice parameters describe the average crystal periodicities, but that superstructure modulations were sometimes observed in *b*-EAO or *o*-EAO ribbons.) The synchrotron results, along with the EDS analyses, clearly show that we have synthesized two new aluminates: tetragonal $EuAl_6O_{10}$ and hexagonal $EuAl_2O_4$.

The lattice structures of the EAO ribbons were confirmed and studied further using spatially-resolved polychromatic X-ray Laue microdiffraction. The X-ray microdiffraction technique is very suitable for determing the new lattice structures of the EAO ribbons, since the great X-ray penetration (tens of micrometers) and high angular resolution (0.01°) enables nondestructive, quantitative measurements of the lattice structures and orientation of the relatively large (200–1000 nm wide and 50–300 nm thick) EAO ribbons. At this facility, a focused polychromatic synchrotron microbeam (diameter, ≈0.5 μm; energy range, ≈6–22 keV) strikes an individual EAO ribbon and the Laue diffraction pattern thus generated is collected by an area detector.[24–26] Indexation of the diffraction peaks in the Laue pattern yields the crystal structure (lattice symmetry) and lattice orientation (e.g., growth axis) of the ribbon. **Figure 3**a shows a *b*-EAO ribbon mounted on a copper TEM grid and Figure 3b shows the Laue microdiffraction pattern acquired from this ribbon. This Laue pattern with more than 500 sharp diffraction peaks can be consistently obtained at any spatial positions of the ribbon and thus reveals the excellent crystal quality of the *b*-EAO ribbon. Essentially all the peaks in the pattern can be indexed using a tetragonal unit cell with lattice parameters of $a = b = 7.77$ Å and $c = 17.30$ Å, which are in good agreement with the synchrotron powder diffraction measurement (Figure 2d). Based on the indexed Laue diffraction pattern, a stereographic projection was created for the *b*-EAO ribbon, as shown in Figure 3c. From Figure 3c the orientation of the *b*-EAO ribbon in Figure 3a can be described as (100) surface plane with [010] along the long growth axis. This common orientation was observed in almost half of the measured tetragonal *b*-EAO ribbons and was associated with a high degree of crystal perfection. Other observed orientations include (110) surface planes with either a [001] or a [1–10] growth axis.

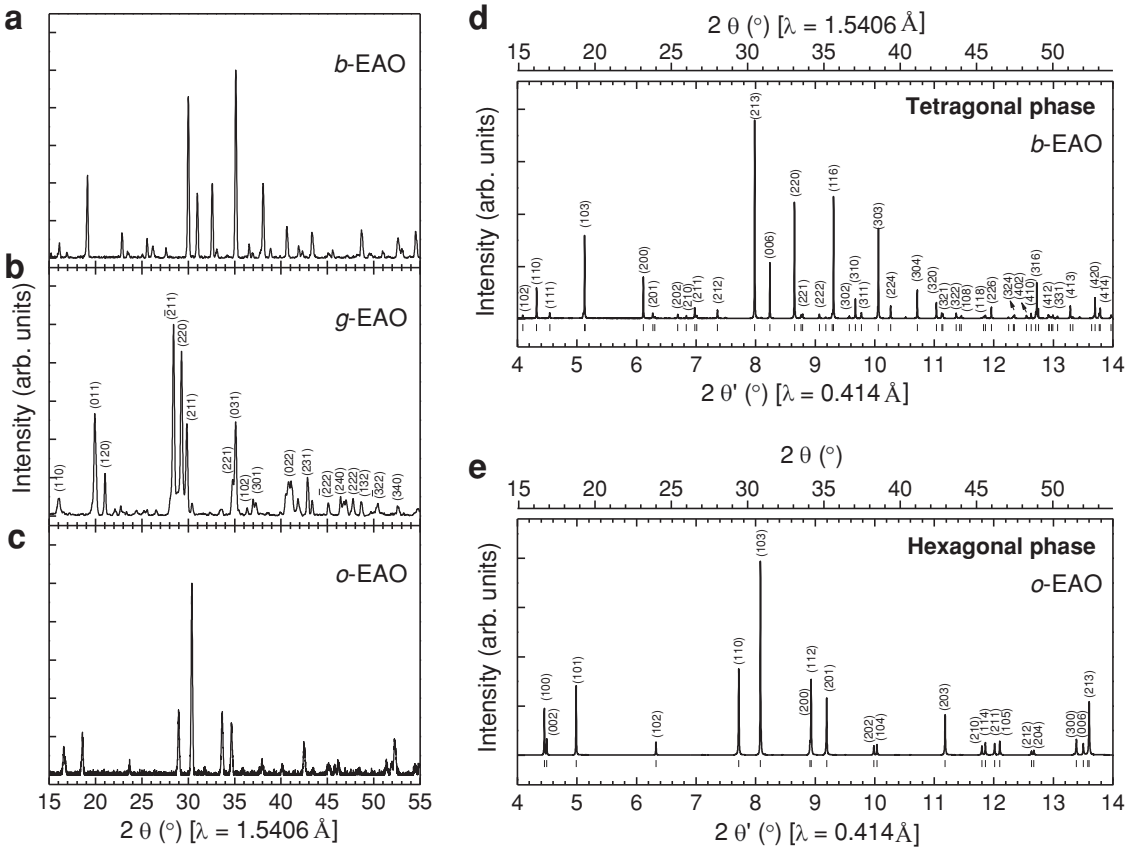

Figure 2. XRD patterns of EAO nanoribbons. a–c) Conventional XRD patterns recorded from *b*-EAO, *g*-EAO and *o*-EAO nanoribbons with Cu Kα_1 radiation (λ = 1.5406 Å). The pattern for *g*-EAO ribbons can be indexed as an isostructure of monoclinic $SrAl_2O_4$ according to JCPDS #34-0379. d,e) Synchrotron X-ray powder diffraction patterns of *b*-EAO and *o*-EAO nanoribbions, respectively, using a monochromatic X-ray beam (λ = 0.414 Å). The tick marks shown below each pattern indicate the peak positions identified by JADE software. The 2θ, and 2θ scales correspond to synchrotron X-ray beam (λ = 0.414 Å) and Cu Kα_1 X-ray beam (λ = 1.5406 Å), respectively.

We also acquired Laue microdiffraction patterns from individual *g*-EAO and *o*-EAO ribbons, as shown in Supporting Information Figure S6 and Figure S7, respectively. The *g*-EAO ribbons can be indexed using a monoclinic unit cell with lattice parameters of a = 8.44 Å, b = 8.82 Å, c = 5.16 Å and β = 93.4°; these values are exactly the same as those of the monoclinic $SrAl_2O_4$ (JCPDS #34-0379). The *o*-EAO ribbons can be indexed using a hexagonal unit cell with lattice parameters of $a = b$ = 6.15 Å and c = 10.57 Å, which are equal to the parameters obtained from powder diffraction measurement (Figure 2e). Analyses on the lattice orientations show that the *g*-EAO ribbons commonly grow along directions about 60°–76° away from the (100) plane normal, while the *o*-EAO ribbons often grow along their hexagonal *c*-axis with (110) plane as the surface normal. However, several other crystallographic orientations were again observed on *g*-EAO and *o*-EAO ribbons, revealing that none of the three types of EAO lattices possess only a single highly-preferred growth axis.

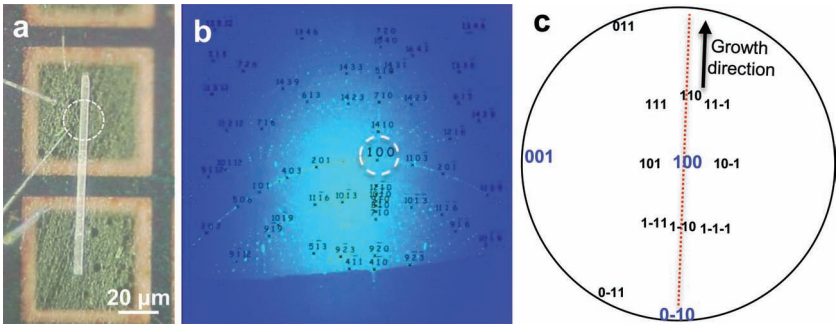

Figure 3. Polychromatic X-ray microdiffraction characterization of a *b*-EAO nanoribbon. a) Optical image of a *b*-EAO ribbon mounted on a copper TEM grid (grid spacing 80 μm) for polychromatic X-ray microdiffraction measurement. The white dashed circle indicates the position where the focused X-ray microbeam (0.5 μm diameter) hits the ribbon. b) Indexed Laue microdiffraction pattern acquired from the *b*-EAO ribbon in a) with the (100) reflection circled. c) Stereographic projection created from the Laue pattern in b) showing that the *b*-EAO ribbon grows along the [010] direction.

It should be noted here that even though the lattice structures, lattice parameters and lattice orientations of the three EAOs can be determined using synchrotron X-ray diffraction techniques, we cannot, at current stage,

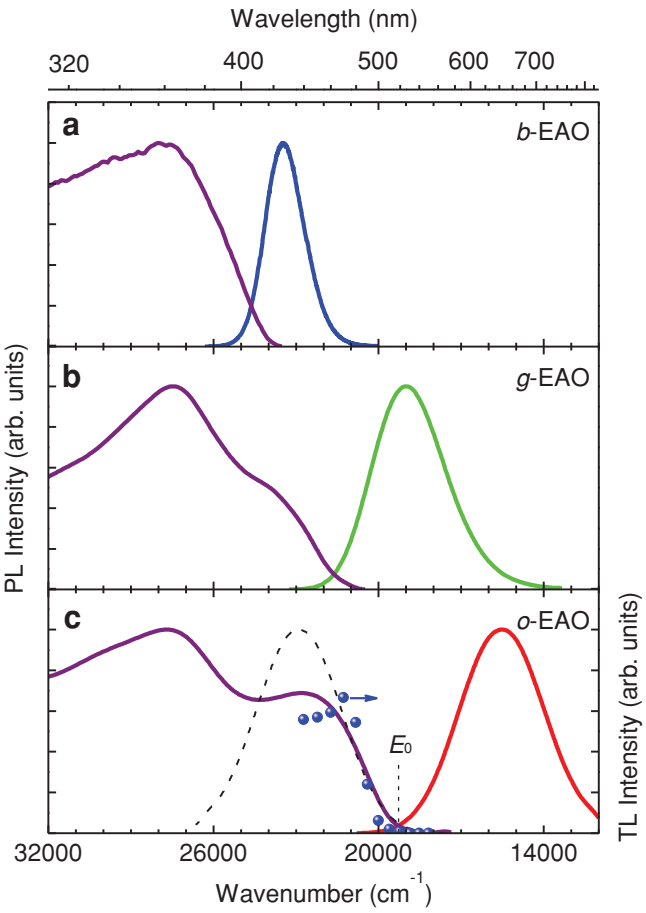

Figure 4. Photoluminescence (PL) spectra and thermoluminescence (TL) intensity of EAO nanoribbons. a–c) Normalized PL excitation and emission spectra of *b*-EAO, *g*-EAO, and *o*-EAO ribbons at room temperature. All the emission spectra are acquired under 365 nm light excitation. The excitation spectra for *b*-EAO, *g*-EAO, and *o*-EAO are obtained by monitoring at 426, 526, and 645 nm emissions, respectively. The dashed line curve in c) is the mirror reflection of the emission band about the zero-phonon line energy E_0. The blue balls in c) represent the TL integrated intensities after excitation with different wavelengths (from 440 to 540 nm) at 77 K in *o*-EAO ribbons.

determine the exact atomic coordinates (e.g., atomic positions, crystallographic space groups and local Eu^{2+} site symmetry) in the materials. These crystallographic information need to be determined in future study because they may provide insights to the understanding of the below discussed novel optical properties possessed by the new EAO materials.

2.4. Luminescence Properties of EAO Nanoribbons

The optical properties of the three luminescent EAO ribbons were studied using spectral methods. Figure 4a–c shows the PL excitation and emission spectra of the three types of EAO ribbons at room temperature. Under 365 nm light excitation, the three EAO ribbons all exhibit broadband emissions but have quite different values for full width at half maximum (FWHM) and Stokes shift of emission (the Stoke shift was roughly estimated as twice of the energy difference between the zero-phonon line energy (E_0) and the peak energy of the emission band;[27] the E_0 was empirically determined as the intersection point of the excitation spectrum and emission spectrum, see, for example, Figure 4c). The blue emission from *b*-EAO ribbons (Figure 4a; peaking at 23 480 cm^{-1}, i.e., ≈426 nm) has a FWHM of 1640 cm^{-1} and a Stokes shift of 2050 cm^{-1}; these values are typical for Eu^{2+}-activated phosphors and can be attributed to normal $4f^65d \rightarrow 4f^7$ transition from Eu^{2+} luminescence centers.[13] The green emission from *g*-EAO ribbons (Figure 4b; peaking at 19 010 cm^{-1}, i.e., ≈526 nm) has a large FWHM of 3040 cm^{-1} and a large Stokes shift of 4390 cm^{-1}, which has been observed in bulk monoclinic $EuAl_2O_4$ and $SrAl_2O_4$:Eu^{2+} phosphors.[22,28] Such broadband green emission was ascribed to the $4f^65d \rightarrow 4f^7$ transition of Eu^{2+} ions, and particularly attributed to the preferential orientation of the Eu^{2+} 5d orbital along the host cation chain in the lattice.[28] Compared with the blue and green emissions, the orange emission from *o*-EAO ribbons (Figure 4c; peaking at 15 500 cm^{-1}, i.e., ≈645 nm) exhibits even larger FWHM (3640 cm^{-1}) and Stokes shift (7440 cm^{-1}). To our best knowledge, both the FWHM and Stokes shift of the orange emission are the largest ever observed in Eu^{2+}-activated aluminate-based materials.[13] These extremely large values suggest that the emission from *o*-EAO ribbons is uncharacteristic of normal Eu^{2+} $4f^65d \rightarrow 4f^7$ transition. In other words, the orange emission may not originate from a generally localized $4f^65d$ emitting level of the Eu^{2+} ion.

To understand the nature of the emitting level in *o*-EAO ribbons, we conducted photoionization experiments based on thermoluminescence (TL) excitation spectroscopy. Figure S8 (Supporting Information) shows a set of TL curves acquired by monitoring 645 nm emission from 77 to 300 K after excitation at 77 K by a monochromatic light in a 10 nm step in the range of 440–540 nm. According to previous reports,[29,30] the TL integrated intensities as a function of excitation wavelengths was plotted to determine the delocalization energy of the impurity electron in *o*-EAO, as the blue balls shown in Figure 4c. It shows that the onset of electron delocalization energy coincides with the onset of PL excitation energy at around 520 nm, revealing the delocalized character of the lowest excited state in *o*-EAO. However, the presence of a strong PL excitation band at 440 nm (≈22 730 cm^{-1}; Figure 4c), which conforms to the "mirror image" (dashed curve in Figure 4c; see Figure S9 of the Supporting Information for further illustration) of the orange emission band, indicates that there exists a large transition moment between the $4f^7$ ground state of the luminescent Eu^{2+} ion and the lowest excited state. According to the dipole selection rule,[31] this means the wave function of the lowest excited state should contain a pronounced localized $4f^65d$ composition. Thus, the lowest excited state (i.e., the emitting state) in *o*-EAO is essentially a $4f^65d$ composition associated with autoionization properties. That is, the lowest excited state is a mixed state consisting of dominating localized $4f^65d$ states and complementary delocalized conduction band-like states. This mixed emitting state was further verified by our luminescence lifetime measurement (Figure S10, Supporting Information), which shows that the radiative lifetime (≈1.27 μs) of the orange emission is close to, but slightly larger than, the characteristic value

(≈1.1 μs) of the normal Eu^{2+} $4f^65d \rightarrow 4f^7$ emission in solids (radiative lifetimes as low as 0.4 μs were also reported in some blue Eu^{2+} phosphors).[32] As a result of electron delocalization in the emitting states, the ligand ions around the luminescent center will undergo a considerable relaxation,[33] which is reflected in the emission spectrum of *o*-EAO by an extremely large FWHM and Stokes shift. It is worth noting that the present emitting state is different from either the delocalized exciton-like state of anomalous luminescence[33] or the localized $4f^65d$ state of normal $4f^65d \rightarrow 4f^7$ transition. The involvement of delocalization in the Eu^{2+} $4f^65d$ emitting state has not been recognized and reported before in Eu^{2+}-activated luminescent materials; thus, it may provide a new insight to the Eu^{2+} luminescence in solids with large bandwidth and large Stokes shift of emission.

2.5. EAO Nanoribbons as Waveguides and White LED Phosphors

The above results show that the three new EAO luminescent nanoribbons exhibit broadband blue, green, and orange emissions from Eu^{2+} ions, and the combination of the three colors covers almost the whole visible spectral region. These luminescent nanomaterials are expected to play significant roles in the development of important emerging optical technologies, for example, as building blocks in nanoscale photonic circuitry or as converting phosphors in light-emitting devices.

We became aware of the potential for using the EAO nanoribbons as light generators and waveguides when we were performing Laue microdiffraction measurements. In addition to diffracted X-ray beams (Figure 3b), strong visible light emission was generated locally at the position where the X-ray beam struck an individual ribbon, and the generated light could propagate hundreds of micrometers along the ribbon and emanate from its ends, as the optical images shown in **Figure 5**a–c (see also Supporting Information Movies S1 to S3). The luminescence colors and emission spectra (Figure S11, Supporting Information) under X-ray excitation are almost the same as those excited by UV light, showing the respective Eu^{2+} emissions in different EAOs as well as the capability of X-ray in exciting these materials. Besides emanating from the ribbon's ends, light was also often observed to scatter in a series of bright spots along the ribbon's length (especially for *g*-EAO, see Figure 5b and Supporting Information Movie S2), which is probably caused by the local nonuniformities along the ribbon.[8] Furthermore, besides the active waveguide feature (i.e., the generated light propagates along the ribbon), the *o*-EAO ribbons also show uniform body emission under point excitation (Figure 5c and Supporting Information Movie S3). The origins of the body luminescence have not been determined yet but it is probably associated with the scattering of the microstructures (e.g., superlattices) in the ribbons. As a result of the body luminescence, the generated light can be routed to other ribbons lying across the emitting one, as the two staggered *o*-EAO ribbons displayed in Figure 5d and the Supporting Information Movie S3. This indicates that the *o*-EAO ribbons can be coupled together to create optical networks. Moreover, the overlap between the emission spectrum of *b*-EAO and the excitation spectra of *g*-EAO and *o*-EAO ribbons (Figure 4) suggests that in an optical network constructed using the three EAO ribbons, it should be possible to use the luminescence from *b*-EAO ribbons to excite the *g*-EAO and *o*-EAO ribbons. This may enable the simultaneous creation, propagation and routing of blue, green, and orange lights in an optical network, and may therefore enhance the network's functionality.

Since the emissions from the three types of EAO ribbons cover almost the whole visible spectral region under near-UV excitation (Figure 4a–c), a combination of the three EAO ribbons with appropriate ratios could be used for the development of phosphor-converted warm-white LEDs, the most promising lighting source for future general illumination.[34–38] Indeed, by carefully tuning the ratios of the three EAO ribbons, we are able to fabricate a series of white light converting phosphors that can produce different white lights when excited with UV (e.g., 365 nm) light. **Figure 6**a–c shows three special white light converting phosphors, labeled as W1, W2, and W3, that were designed to combine with a 365-nm UV LED to produce, respectively, the CIE standard illuminant D65 (i.e., average daylight having a correlated color temperature (CCT) of approximately 6500 K),[37] "warm" white light (CCT <4000 K), and standard illuminant A (i.e., typical, domestic, tungsten-filament lighting with CCT of approximately 2856 K).[35] The emission spectra of these three white light phosphors under 365 nm light excitation are shown in Figure 6d. Figure 6e is the CIE 1931 chromaticity diagram showing the color point positions of the three white light spectra (labeled as red crosses), the illuminant D65 and illuminant A (labeled as black dots), as

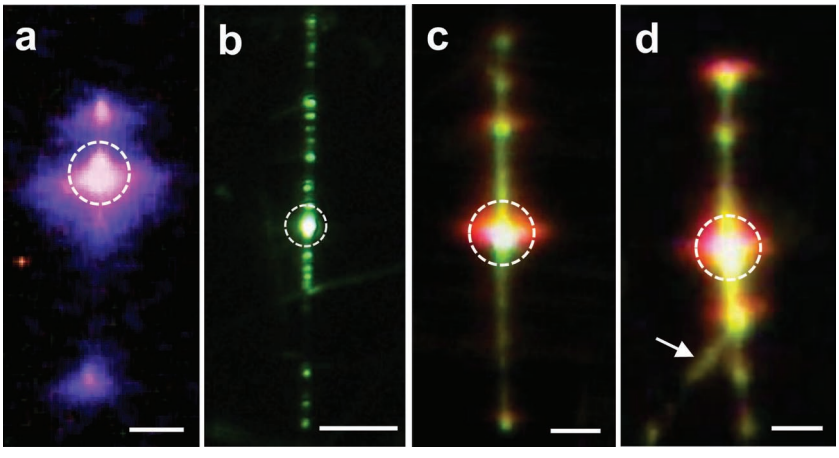

Figure 5. EAO nanoribbon waveguides with X-ray excitation. a–c) Optical images showing the generation and propagation of light by individual *b*-EAO ribbon, *g*-EAO ribbon, and *o*-EAO ribbon when the ribbon was struck by a focused X-ray beam (diameter ≈ 0.5 μm). The beam positions are indicated by white dashed circles. The ribbons were mounted on copper TEM grids. The *b*-EAO ribbon in a) is the same as the one in Figure 3a. d) Optical image of two staggered *o*-EAO nanoribbons, showing the X-ray excited orange light in a long ribbon emanating along the ribbon body and routing to a short ribbon (indicated by a white arrow head) lying on it. The X-ray beam position is indicated by a white dashed circle. The scale bars are 20 μm.

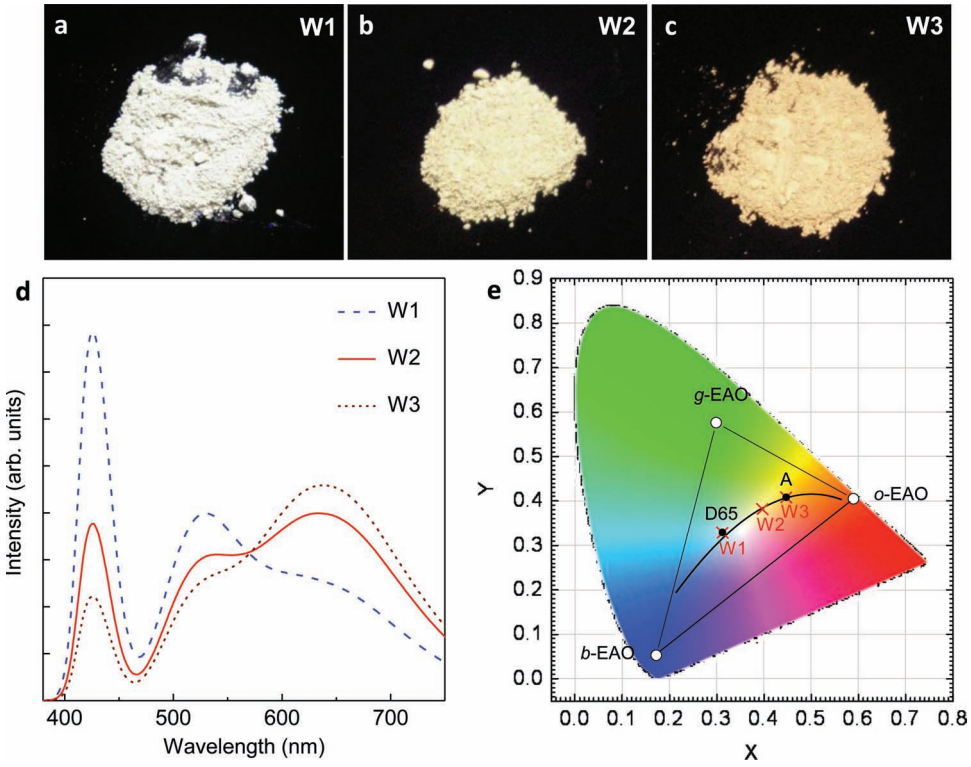

Figure 6. White lights created by the combination of *b*-EAO, *g*-EAO, and *o*-EAO nanoribbons. a–c) Optical images of three white light converting phosphors created by mixing *b*-EAO, *g*-EAO, and *o*-EAO ribbons at certain ratios. These three phosphors were designed to combine with a 365-nm UV LED to produce: a) CIE standard illuminant D65 (W1); b) warm white light (W2); and c) standard illuminant A (W3). The images were taken by a digital camera under the illumination of a 365-nm UV lamp in a dark room. d) Emission spectra of the three white light converting phosphors under the excitation of 365 nm light. e) Chromaticity coordinates in CIE 1931 diagram. White dots represent the color points of the emissions from *b*-EAO, *g*-EAO, and *o*-EAO ribbons. Black dots are the color points of illuminant D65 and illuminant A. The three red crosses represent the color points of the three spectra in d). The black solid curve is the Planckian locus. The CCT values for W1, W2, and W3 are about 6500, 3500, and 2900 K, respectively. The corresponding CRI values are about 81, 93 and 90, respectively. The CIE 1931 color space chromaticity coordinates for W1, W2, and W3 are (0.313, 0.329), (0.399, 0.382), and (0.448, 0.407), respectively.

well as the three EAOs (labeled as white dots). The color points of mixed phosphors W1 and W3 perfectly coincide with that of illuminant D65 and illuminant A, respectively, showing that we can precisely tune the ratios of the three EAOs. The obtained CCT and color rendering index (CRI) for mixed phosphor W2 are 3500 K and 93, respectively. These values fall perfectly in the ranges for desired warm-white light (CCT = 2580–3710 K and CRI >85) defined by the U.S. Department of Energy.[38] These results indicate that it is possible to achieve warm-white LEDs for general illumination based on all-europium aluminate phosphors.

It should be noted here that despite the desirable CCT and CRI values for general illumination, the EAO materials face several weaknesses for practical applications. For example, the luminous efficacy rate of the combined emission spectrum for the white lights is expected to be not very high, due to the contribution of emission above 700 nm (see Figure 6d) where the eye sensitivity is low. In addition, the luminescence quantum efficiencies (QE) of present materials are not very satisfactory with the measured QEs of *b*-EAO, *g*-EAO, and *o*-EAO being about 18%, 31%, and 34%, respectively, under 365 nm excitation at room temperature. Several factors are possibly responsible for the relatively low QEs. First, the effect of concentration quenching is inevitable in the present fully concentrated phosphors, especially for *b*-EAO, in which the energy migration is efficient due to the small Stokes shift of emission. In *g*-EAO and *o*-EAO, even though the large Stokes shifts of emissions reduce the effect of concentration quenching due to the restriction of energy migrations, they can cause more relaxation loss and thus can lower the QEs.[22] Second, the thermal quenching of luminescence starting bellow room temperature may also contribute to the reduction of QEs (see, for example, Figure S10 of the Supporting Information).[39] Third, some local defects introduced in the fabrication stage may act as luminescence quenching centers, which may further lower the QEs. Nevertheless, since these materials are new, we believe that a better understanding of the underlying luminescence mechanisms and further improvement of the synthesis processes may lead to a significant increase in their QEs.

3. Conclusions

In summary, by using a modified and strictly controlled carbothermal reaction and evaporation method, we have fabricated Eu^{2+}-activated phosphors into 1D nanostructures and

successfully synthesized three new ternary europium aluminate nanoribbons with new compositions, new crystal lattice structures, and new luminescence properties and mechanisms. The reported method is new but general and can be used to synthesize many other, new, and more complicated Eu^{2+}-activated aluminate nanoribbons, as well as other rare earth ion-activated luminescent nanostructures. For example, we have also synthesized three kinds of quaternary strontium europium aluminate nanoribbons with luminescence colors of blue, green, and yellow, and four kinds of quaternary barium europium aluminate nanoribbons with luminescence colors of blue, green, yellow, and red.[19] Thus, our method opens a new avenue for the synthesis of new, rare earth ion-activated, multi-component luminescent nanomaterials for applications in emerging optical technologies.

4. Experimental Section

Fabrication of EAO Nanoribbons: The EAO nanoribbons were synthesized by carbothermal reaction and evaporation of a mixture of Eu_2O_3, Al_2O_3 and graphite powders in a tube furnace system (Supporting Information, Figure S1a). For the synthesis of *g*-EAO and *o*-EAO ribbons, Eu_2O_3, Al_2O_3 and graphite powders with mass ratio of ≈0.6/0.1/1 were ground thoroughly and transferred into an alumina boat. The boat was then positioned at the center of an alumina tube that was inserted into a horizontal tube furnace. An alumina plate (≈15-mm wide and 60-mm long) was placed downstream to act as nanoribbon-growth substrate. After the alumina tube was pumped to $\approx 2 \times 10^{-3}$ Torr, the source powders were heated to 1450 °C at a rate of 15 °C/min under an argon atmosphere at a flow rate of 50 sccm and a pressure of about 5 Torr. The reaction lasted for 2 h. For the synthesis of *b*-EAO ribbons, the Eu_2O_3:Al_2O_3:graphite mass ratio was changed to ≈0.6:0.5:1, the argon pressure was increased to 10–15 Torr, and other parameters kept unchanged.

Characterization of Morphology and Compositions: The morphology and compositions of the as-synthesized nanoribbons were characterized by SEM (FEI Inspect F FEG-SEM), TEM (Hitachi HF-3300 FEG TEM/STEM), and EDS (EDAX GENESIS XM 2) attached to the SEM.

X-ray Absorption Near Edge Structure (XANES) Measurements: The XANES measurements on Eu L_3 edge were performed at room temperature using linear polarized X-ray at the APS beamline 20-BM-B. A multi-element Ge detector was used to select the Eu fluorescence for counting.

Powder X-ray Diffraction Measurements: The crystal structures of the EAO nanoribbons were recorded by both a conventional powder X-ray diffractometer with Cu Kα_1 radiation (λ = 1.5406 Å; PANalytical X'Pert PRO) and synchrotron powder X-ray diffraction. The latter measurement was conducted on the beamline 11-BM-B at the APS. The nanoribbons were encapsulated inside a narrow capillary tube and irradiated by a monochromatic X-ray beam (λ = 0.414 Å). The diffraction patterns were fit by JADE diffraction analysis software to identify the phases and lattice parameters.

Synchrotron X-ray Laue Microdiffraction Measurements: The synchrotron X-ray Laue microdiffraction studies were conducted at APS beamline 34-ID-E.[24–26] In this approach, a pair of curved Kirkpatrick-Baez reflecting mirrors was used to focus an intense synchrotron X-ray beam with a broad energy range (≈6–22 keV) onto the sample with a beam diameter of ≈0.5 μm. The nanoribbons were mounted on a Cu TEM grid which can be precisely translated along the *X*–*Y* plane with respect to the microbeam so that the microbeam can scan individual nanoribbon over its length or width. Scattering of the polychromatic beam generated a Laue diffraction pattern, consisting of many diffraction peaks, each satisfying Bragg's law for a different set of *hkl* crystal planes. The Laue diffraction pattern was collected using a large area CCD detector. In addition to the diffracted beams, intense visible light emission was generated locally at the position where the X-ray beam struck the ribbon. By optically imaging the samples with a high-resolution television camera, we observed the generation and propagation of light by individual ribbons. By collecting the luminescence using a fiberoptic-coupled optical spectrometer, we obtained X-ray excited emission spectra from individual ribbons.

Luminescence Property Measurements: The PL excitation and emission spectra were acquired using a HORIBA Jobin Yvon Fluorolog-3 spectrofluorometer equipped with a 450 W xenon lamp as the excitation source. The TL curves were recorded using the Fluorolog-3 spectrofluorometer and a homemade TL setup consisting of a Dewar bottle, a copper sample holder, a cartridge heater and an Omega temperature controller. The measurement was carried out by illuminating the *o*-EAO sample at 77 K for 10 min with a monochromatic light from the xenon lamp, in a 10-nm step in the range of 440 and 540 nm. Prior to each measurement, the sample was heated to 400 K to empty the electron traps. After each illumination, the TL emission signal, monitored at 645 nm, was recorded from 77 to 300 K at a linear heating rate of 4 K/s. The diffuse reflectance absorption was measured using a Shimadzu UV-2450 UV-vis spectrometer. The luminescence lifetime was recorded using a photomultiplier tube and a digital oscilloscope under excitation with the third harmonic (355 nm) of a Nd:YAG pulsed laser. The luminescence quantum efficiency was measured using a quantum yield accessory attached to the spectrofluorometer. In all optical measurements, appropriate optical filters were used to avoid stray light.

Supporting Information

Supporting Information is available from the Wiley Online Library or from the author.

Acknowledgements

Z.W.P. acknowledges funding support from the National Science Foundation (CAREER DMR-0955908). J.D.B. and J.Z.T. were supported by the Materials Sciences and Engineering Division, Office of Basic Energy Sciences (BES), U.S. Department of Energy (DOE). Use of the APS beamline 11-BM-B for synchrotron X-ray powder diffraction and beamline 34-ID-E for polychromatic Laue microdiffraction was supported by the Scientific User Facilities Division of BES, U.S. DOE. Use of the APS beamline 20-BM-B for XANES measurement by C.J.S. was supported by U.S. DOE under Contract No. DE-AC02-06CH11357 with Argonne National Laboratory. The TEM characterization was conducted at the Oak Ridge National Laboratory ShaRE User Facilities, which is sponsored by the Division of Scientific User Facilities of BES, U.S. DOE.

Received: September 4, 2012
Revised: October 16, 2012
Published online: November 15, 2012

[1] F. Qian, Y. Li, S. Gradecak, D. L. Wang, C. J. Barrelet, C. M. Lieber, *Nano Lett.* **2004**, *4*, 1975.
[2] Y. Huang, X. F. Duan, C. M. Lieber, *Small* **2005**, *1*, 142.
[3] M. H. Huang, S. Mao, H. Feick, H. Q. Yan, Y. Y. Wu, H. Kind, E. Weber, R. Russo, P. D. Yang, *Science* **2001**, *292*, 1897.
[4] X. F. Duan, Y. Huang, R. Agarwal, C. M. Lieber, *Nature* **2003**, *421*, 241.
[5] D. J. Sirbuly, M. Law, P. Pauzauskie, H. Q. Yan, A. V. Maslov, K. Knutsen, C. Z. Ning, R. J. Saykally, P. D. Yang, *Proc. Natl. Acad. Sci. USA* **2005**, *102*, 7800.
[6] Q. Wan, Q. H. Li, Y. J. Chen, T. H. Wang, X. L. He, J. P. Li, C. L. Lin, *Appl. Phys. Lett.* **2004**, *84*, 3654.

[7] C. J. Barrelet, A. B. Greytak, C. M. Lieber, *Nano Lett.* **2004**, *4*, 1981.
[8] M. Law, D. J. Sirbuly, J. C. Johnson, J. Goldberger, R. J. Saykally, P. D. Yang, *Science* **2004**, *305*, 1269.
[9] G. K. Liu, B. Jacquier, *Spectroscopic Properties of Rare Earths in Optical Materials*, Springer Verlag, Berlin **2005**.
[10] T. Jüstel, H. Nikol, C. Ronda, *Angew. Chem. Int. Ed.* **1998**, *37*, 3084.
[11] J. C. G. Bünzli, C. Piguet, *Chem. Soc. Rev.* **2005**, *34*, 1048.
[12] P. Escribano, B. Julian-Lopez, J. Planelles-Arago, E. Cordoncillo, B. Viana, C. Sanchez, *J. Mater. Chem.* **2008**, *18*, 23.
[13] P. Dorenbos, *J. Lumin.* **2003**, *104*, 239.
[14] A. A. Setlur, *Electrochem. Soc. Interface* **2009**, *18*, 32.
[15] R. J. Xie, N. Hirosaki, T. Takeda, *Appl. Phys. Express* **2009**, *2*, 022401.
[16] S. Schweizer, *Phys. Status Solidi A* **2001**, *187*, 335.
[17] T. Matsuzawa, Y. Aoki, N. Takeuchi, Y. Murayama, *J. Electrochem. Soc.* **1996**, *143*, 2670.
[18] J. Selling, M. D. Birowosuto, P. Dorenbos, S. Schweizer, *J. Appl. Phys.* **2007**, *101*, 034901.
[19] Z. W. Pan, F. Liu, X. F. Li, US Patent 11/24268, **2011**.
[20] Z. W. Pan, Z. R. Dai, Z. L. Wang, *Science* **2001**, *291*, 1947.
[21] S. M. Heald, D. L. Brewe, E. A. Stern, K. H. Kim, F. C. Brown, D. T. Jiang, E. D. Crozier, R. A. Gordon, *J. Synchrotron Radiat.* **1999**, *6*, 347.
[22] G. Schierning, M. Batentschuk, A. Osvet, A. Stiegelschmitt, A. Winnacker, *Phys. Status Solidi C* **2005**, *2*, 109.
[23] J. Wang, B. H. Toby, P. L. Lee, L. Ribaud, S. M. Antao, C. Kurtz, M. Ramanathan, R. B. von Dreele, M. A. Beno, *Rev. Sci. Instrum.* **2008**, *79*, 085105.
[24] B. C. Larson, W. G. Yang, G. E. Ice, J. D. Budai, J. Z. Tischler, *Nature* **2002**, *415*, 887.
[25] J. D. Budai, W. G. Yang, N. Tamura, J. S. Chung, J. Z. Tischler, B. C. Larson, G. E. Ice, C. Park, D. P. Norton, *Nat. Mater.* **2003**, *2*, 487.
[26] G. E. Ice, J. D. Budai, W. L. Pang, *Science* **2011**, *334*, 1234.
[27] V. Bachmann, T. Jüstel, A. Meijerink, C. Ronda, P. J. Schmidt, *J. Lumin.* **2006**, *121*, 441.
[28] S. H. M. Poort, W. P. Blokpoel, G. Blasse, *Chem. Mater.* **1995**, *7*, 1547.
[29] J. Fleniken, J. Wang, J. Grimm, M. J. Weber, U. Happek, *J. Lumin.* **2001**, *94–95*, 465.
[30] J. Grimm, J. Fleniken, K. W. Kraemer, D. Biner, U. Happek, H. U. Guedel, *J. Lumin.* **2007**, *122–123*, 325.
[31] C. Pédrini, M. F. Joubert, D. S. McClure, *J. Lumin.* **2007**, *125*, 230.
[32] S. H. M. Poort, A. Meijerink, G. Blasse, *J. Phys. Chem. Solids* **1997**, *58*, 1451.
[33] P. Dorenbos, *J. Phys.: Condens. Matter* **2003**, *15*, 2645.
[34] E. F. Schubert, J. K. Kim, *Science* **2005**, *308*, 1274.
[35] S. Pimputkar, J. S. Speck, S. P. DenBaars, S. Nakamura, *Nat. Photonics* **2009**, *3*, 179.
[36] S. Ye, F. Xiao, Y. X. Pan, Y. Y. Ma, Q. Y. Zhang, *Mater. Sci. Eng. R* **2010**, *71*, 1.
[37] E. F. Schubert, *Light-Emitting Diodes*, Cambridge University Press, Cambridge **2006**.
[38] US Department of Energy, *Solid-State Lighting Research and Development: Multi-Year Program Plan*, US DOE, Washington, DC **2011**.
[39] P. Dorenbos, *J. Phys.: Condens. Matter* **2005**, *17*, 8103.